

# H<sub>3</sub><sup>+</sup> in Diffuse Interstellar Clouds: A Tracer for the Cosmic-Ray Ionization Rate

Nick Indriolo<sup>1</sup>, Thomas R. Geballe<sup>2</sup>, Takeshi Oka<sup>3</sup>, and Benjamin J. McCall<sup>1</sup>

## ABSTRACT

Using high resolution infrared spectroscopy we have surveyed twenty sightlines for H<sub>3</sub><sup>+</sup> absorption. H<sub>3</sub><sup>+</sup> is detected in eight diffuse cloud sightlines with column densities varying from  $0.6 \times 10^{14}$  cm<sup>-2</sup> to  $3.9 \times 10^{14}$  cm<sup>-2</sup>. This brings to fourteen the total number of diffuse cloud sightlines where H<sub>3</sub><sup>+</sup> has been detected. These detections are mostly along sightlines concentrated in the Galactic plane, but well dispersed in Galactic longitude. The results imply that abundant H<sub>3</sub><sup>+</sup> is common in the diffuse interstellar medium. Because of the simple chemistry associated with H<sub>3</sub><sup>+</sup> production and destruction, these column density measurements can be used in concert with various other data to infer the primary cosmic-ray ionization rate,  $\zeta_p$ . Values range from  $0.5 \times 10^{-16}$  s<sup>-1</sup> to  $3 \times 10^{-16}$  s<sup>-1</sup> with an average of  $2 \times 10^{-16}$  s<sup>-1</sup>. Where H<sub>3</sub><sup>+</sup> is not detected the upper limits on the ionization rate are consistent with this range. The average value of  $\zeta_p$  is about an order of magnitude larger than both the canonical rate and rates previously reported by other groups using measurements of OH and HD. The discrepancy is most likely due to inaccurate measurements of rate constants and the omission of effects which were unknown when those studies were performed. We believe that the observed column density of H<sub>3</sub><sup>+</sup> is the most direct tracer for the cosmic-ray ionization rate due to its simple chemistry. Recent models of diffuse cloud chemistry require cosmic-ray ionization rates on the order of 10<sup>-16</sup> s<sup>-1</sup> to reproduce observed abundances of various atomic and molecular species, in rough accord with our observational findings.

*Subject headings:* astrochemistry – cosmic rays – ISM: clouds – ISM: molecules

---

<sup>1</sup>Department of Astronomy and Department of Chemistry, University of Illinois at Urbana-Champaign, Urbana, IL 61801; nindrio2@uiuc.edu, bjmccall@uiuc.edu

<sup>2</sup>Gemini Observatory, 670 North A'ohoku Place, Hilo, HI 96720

<sup>3</sup>Department of Astronomy & Astrophysics and Department of Chemistry, University of Chicago, Chicago, IL 60637

## 1. INTRODUCTION

In the past several years  $\text{H}_3^+$  has been detected in diffuse interstellar clouds (McCall et al. 1998, 2002; Geballe et al. 1999) where it had been expected to exist in abundances below observable limits. This surprising result raised various questions about the diffuse cloud environment. The rather simple chemistry of  $\text{H}_3^+$  allows for only three variable parameters in determining its abundance when the steady state approximation is used: the  $\text{H}_3^+$ -electron recombination rate, the electron to hydrogen ratio, and the cosmic-ray ionization rate. Previous work (McCall et al. 2003, 2004; Cardelli et al. 1996) has shown that the first two of these are relatively well constrained. This leaves the cosmic-ray ionization rate as an unconstrained parameter. Because the low energy cosmic-rays responsible for most of the ionization in diffuse clouds cannot be directly measured in the solar system, we must rely on molecules to act as tracers of the ionization rate. Using  $\text{H}_3^+$ , McCall et al. (2003) found the cosmic-ray ionization rate of molecular hydrogen,  $\zeta_2$ , to be much larger along the sightline to  $\zeta$  Per than the canonical value of  $\sim 3 \times 10^{-17} \text{ s}^{-1}$ .

Prior to the detection of  $\text{H}_3^+$  in diffuse clouds, OH and HD were the molecules of choice for estimating the cosmic-ray ionization rate there. Estimates using these molecules required determining rate constants and modeling various reactions on the pathways to forming OH and HD (Black & Dalgarno 1977; Federman et al. 1996; O'Donnell & Watson 1974). The derived values of the ionization rate tended to agree with the canonical value of  $\zeta_p$ , the primary cosmic-ray ionization rate, but differ greatly from the value derived from the recent  $\text{H}_3^+$  measurement toward  $\zeta$  Per (the relation between  $\zeta_p$  and  $\zeta_2$  is explained in § 4.2 and quantified by equation (10)). Of the three molecules, the simple chemistry of  $\text{H}_3^+$  provides the most direct determination of  $\zeta_p$  (Dalgarno 2006), suggesting that measurements of  $\text{H}_3^+$  should produce more accurate results and be a more reliable tracer of the cosmic-ray ionization rate than OH or HD.

The higher ionization rate found by McCall et al. (2003) towards  $\zeta$  Per implies the production of more  $\text{H}_3^+$ , and if generally applicable, could account for the higher than expected column densities found in several diffuse clouds (McCall et al. 2002). However, prior to the present work the enhanced ionization rate was known to exist for certain only along one line of sight, and thus could have been considered an anomaly. To test if an enhanced ionization rate is a general property of the diffuse interstellar medium (ISM), we have performed a survey of  $\text{H}_3^+$  in nineteen diffuse cloud sightlines.  $\text{H}_3^+$  is detected in eight of the clouds and the overall results, including analysis of previous observations by our group, support a higher ionization rate. When coupled with further arguments, this strongly suggests that a greatly enhanced ionization rate is a typical property of the diffuse ISM.

## 2. METHODS

### 2.1. Observations

All observations were made using the CGS4 spectrometer (Mountain et al. 1990) on the United Kingdom Infrared Telescope (UKIRT) at Mauna Kea. The spectrometer was used with its echelle grating, 0.6 arcsec wide slit, and long camera to provide a resolving power of 40000. Observations were taken in an ABBA pattern in which the target star is nodded along the slit so that the spectral image falls alternately on different rows of the array. Suitable standard stars were observed throughout each night to account for changing atmospheric conditions and air mass. With the exception of the Red Rectangle where reddening is due to the ejected envelope of a post asymptotic giant branch star, targets were chosen primarily by three criteria: (1) sightlines known to pass through diffuse clouds; (2) early spectral type; and (3) bright L-band magnitude. The complete dataset consists of twenty (nineteen diffuse cloud) sightlines which were observed intermittently between May 2001 and March 2005. Relevant information concerning these observations is given in Table 1. Two of the sightlines from the dataset were examined in McCall et al. (2002): HD 20041 and  $\zeta$  Oph. However, both have previously been studied using only the  $R(1, 1)^l$  transition at 37154.8 Å (vacuum wavelengths are used throughout this paper), whereas the new data cover the  $R(1, 1)^u$  and  $R(1, 0)$  transitions at 36680.8 Å and 36685.2 Å, respectively (see McCall (2000) or McCall & Oka (2000) for a complete description of the transition notation associated with  $H_3^+$ ).  $\zeta$  Per was investigated in McCall et al. (2003), but here data from three more nights of observations are included. Overall, we present twenty sightlines for which new or refined  $H_3^+$  column densities or upper limits are calculated.

### 2.2. Data Reduction

The reduction process involves multiple steps and software packages. First, raw data are run through Starlink’s ORAC-DR<sup>1</sup> pipeline which processes UKIRT data. Images are then transformed to fits format using Starlink’s FIGARO<sup>2</sup> package, and neighboring images are subtracted from each other in NOAO’s IRAF<sup>3</sup> package. This subtraction serves to eliminate atmospheric background and detector bias levels from the image. Still using IRAF, spectra

---

<sup>1</sup><http://www.oracdr.org/>

<sup>2</sup><http://www.starlink.rl.ac.uk/star/docs/sun86.htm/sun86.html>

<sup>3</sup><http://iraf.noao.edu/>

are extracted from the neighbor-subtracted images with the *apall* routine. These spectra are imported to IGOR Pro<sup>4</sup> where we have macros set up to complete the reduction (McCall 2001). During this import, ripples in the spectrum caused by guiding and seeing fluctuations while the CGS4 array is shifted along the spectral direction in successive steps of one-third of a pixel during observing are removed. Spectra for each object and standard star are then coadded. Some frames may be excluded in this step if they are noisier than normal or happen to have cosmic-ray hits on the rows where the spectrum is located. Objects are then ratioed with standards to remove atmospheric absorption lines and the continuum level is set to unity. The ratioing is an interactive process where the user may vary the intensity scaling and/or shift the spectrum in wavelength in order to most effectively remove atmospheric lines and obtain the most reliable ratioed spectrum at the wavelengths where the H<sub>3</sub><sup>+</sup> lines are expected to appear. A fringing pattern caused by the circular variable order-blocking filter is another artifact of CGS4 that needs to be removed. This is accomplished by transforming a spectrum into Fourier space using an IGOR macro. The user can then find the peak caused by the fringing pattern and interpolate across it. Once the peak is removed, an inverse Fourier transform is performed to produce a spectrum where the fringing pattern is absent. This method is described in more depth in McCall (2001). After removing the fringing pattern, spectra are wavelength calibrated using the vacuum rest wavelengths of the atmospheric lines. The accuracy of the wavelength calibration is typically  $\pm 2 \text{ km s}^{-1}$ . Finally, the H<sub>3</sub><sup>+</sup> lines are fit with Gaussians and the equivalent widths, column densities, and radial velocities are derived.

For targets with observations on multiple nights, the reduction process above is followed through the wavelength calibration step. At that point IRAF’s *rvcorrect* routine is used to calculate the velocity of the Earth along a given sightline in the local standard of rest (LSR) frame. Each spectrum is then shifted to be in the LSR frame. This puts the interstellar absorption lines at the same wavelength for any given date and allows spectra from different nights to be coadded. While each spectrum has its continuum set to unity, they originally had different exposure times and intensities. To weight the final coadded spectrum properly, each spectrum is scaled by its original coadded intensity before being added to the spectra from other nights. Once the final multiple night coadded spectrum is produced, it is divided by the sum of the scaling factors to reset the continuum level to unity. After this process, line parameters are again extracted by fitting the absorption lines.

---

<sup>4</sup><http://www.wavemetrics.com/>

### 2.3. Atmospheric Interference

Spectra covering the  $\text{H}_3^+$  doublet are adversely affected by an atmospheric  $\text{CH}_4$  line complex which lies just shortward of 36680.8 Å, the rest wavelength of the  $R(1,1)^u$  line. If the spectrum of the target is blue-shifted, the overlap with this line can be significant and hinder detection or estimates of line strength. Typical examples of spectra before the atmospheric lines are removed via ratioing with a standard star are shown in Figure 1. The  $\text{CH}_4$  feature here absorbs roughly 50% of the incoming light at 36675.3 Å in both the standard star  $\beta$  Per (middle spectrum) and the object  $\zeta$  Per (bottom spectrum). A weak telluric HDO absorption line near 36681 Å that can vary with both time and airmass further complicates the reduction, especially when the water column density above the telescope is high and unstable. When the two spectra are ratioed following the methods in § 2.2, the top spectrum in Figure 1 is produced. The two lines show the rest wavelength positions of the  $R(1,1)^u$  line at 36680.8 Å and the  $R(1,0)$  line at 36685.2 Å. Two arrows mark the expected positions of the  $\text{H}_3^+$  lines due the Earth’s orbital motion and the radial velocity of the absorbing cloud along the line of sight towards  $\zeta$  Per. Clearly the  $\text{H}_3^+$  absorption lines are much weaker than the atmospheric absorption lines and are barely visible at this scaling factor. This illustrates why a careful multi-step reduction process is necessary to detect  $\text{H}_3^+$ .

## 3. RESULTS

### 3.1. Positive Detections

The fully reduced spectra are shown in Figures 2-5. Figures 2 and 3 contain spectra from sightlines with positive  $\text{H}_3^+$  detections, and Figures 4 and 5 show spectra from sightlines with no  $\text{H}_3^+$  detections or marginal detections. Arrows indicate the position of the  $\text{H}_3^+$  doublet expected from previous measurements of the gas velocity along each line of sight. These velocities are given in Table 2 along with the atomic or molecular species from which they were determined. In the figures the typical noise level can be judged by the peak-to-peak fluctuations in the continuum well off of the  $\text{H}_3^+$  lines. Within several Ångströms of 36675.3 Å, however, the noise in the reduced spectra is several times larger than elsewhere due to the presence of the strong complex of  $\text{CH}_4$  lines, which both reduces the atmospheric transmission and emits excess background.

The three spectra in Figure 2 have the strongest  $\text{H}_3^+$  absorption. In each case the lines match up with the arrows so we are confident in the  $\text{H}_3^+$  detection. In HD 20041 the  $R(1,0)$  transition is clearly visible but the  $R(1,1)^u$  transition may have been affected by the aforementioned  $\text{CH}_4$  line. Both absorption lines are clear and strong in HD 229059.

W40 IRS 1a presents a somewhat confusing case because there may be either one or two velocity components. If there is one component, then the two absorption lines to longer wavelengths represent the  $H_3^+$  doublet and the shorter wavelength line at 36677 Å is a noise artifact. If there are two absorption components, then the  $R(1, 0)$  transition from the shorter wavelength doublet overlaps the  $R(1, 1)^u$  transition from the longer wavelength doublet. However, the W40 IRS 1a spectrum is composed of data from two nights and on only one of those nights does the 36677 Å feature appear. For this reason we conclude that only the longer wavelength doublet is real. Our conclusion is consistent with the observations reported by Crutcher & Chu (1982) in which only one velocity component at about 8 km s<sup>-1</sup> LSR was seen in <sup>13</sup>CO emission, but does not match the 2±2 km s<sup>-1</sup> LSR reported by Shuping et al. (1999) from <sup>12</sup>CO absorption. Note, however, that if the other line is real then it would correspond to a cloud with a radial velocity of about -30 km s<sup>-1</sup> LSR, which disagrees badly with both CO measurements.

In Figure 3 the absorption lines are again aligned with the arrows marking previously observed gas velocities.  $\zeta$  Per and HD 21389 have the highest signal to noise ratios (SNR) and their  $H_3^+$  lines are easily identified. The doublet in X Per is relatively clear, but the velocities found by fitting the individual line profiles differ by 2.5 km s<sup>-1</sup>. Most likely this is due to noise affecting the absorption feature. In HD 169454 the  $R(1, 0)$  transition of the main doublet is clear, but the  $R(1, 1)^u$  line is rather shallow. As in the case of HD 20041 above, this may be caused by interference from the telluric CH<sub>4</sub> line. However, the velocity we derive for the  $R(1, 0)$  transition differs from the previously measured cloud velocity by about 3.2 km s<sup>-1</sup>. Because of the different velocities and the lack of a clear  $R(1, 1)^u$  line, we are not as confident as in the previous cases that these features represent  $H_3^+$  absorption, but still consider it a positive detection. The shorter arrows above the HD 169454 spectrum mark the expected location of the  $H_3^+$  doublet for a high velocity component at 90 km s<sup>-1</sup> reported by Federman & Lambert (1992). Our spectrum may indicate absorption features at this velocity, but further integration time is needed to determine if the features are real. The absorption features in BD -14 5037 both appear to be double peaked, although the signal-to-noise ratio of each double peak is low. It also seems that there are small absorption features on the shorter wavelength shoulders of the main features. Two velocity components reported by Gredel & Münch (1986) match well with the centers of the double peaked features and the shoulder features, making the detections more believable.

### 3.2. Negative Detections

There is no definitive evidence for  $\text{H}_3^+$  absorption lines in any spectrum in Figure 4, with the possible exception of *o* Per. The arrow marking the  $R(1, 0)$  transition of  $\text{H}_3^+$  in *o* Per matches rather well with a statistically significant absorption feature in the spectrum. However, at the expected wavelength of the  $R(1, 1)^u$  line the absorption is too weak to attempt a fit given the noise level. Both  $\xi$  Per and  $\epsilon$  Per show some amount of absorption near the wavelengths where the  $\text{H}_3^+$  lines are expected, but nothing that can be conclusively identified as a detection. The Red Rectangle and  $\zeta$  Oph sightlines both have a very high SNR. With these clean spectra and no  $\text{H}_3^+$  absorption, it is possible to derive strict upper limits. HD 147889, 40 Per, and *o* Sco all have no significant absorption features close to the expected wavelengths. Figure 5 contains two non-detections in spectra with typical noise levels (HD 168625 and  $\lambda$  Cep) and two with high noise levels (HD 21483 and 62 Tau).

## 4. ANALYSIS

By fitting the absorption lines in the spectra with Gaussians we are able to obtain the line of sight velocity, full width at half maximum, equivalent width, and the  $\text{H}_3^+$  column density and its uncertainty. Values for these parameters along all of the observed sightlines are given in Table 3. Using these values in concert with the steady state approximation and a few reasonable assumptions allows for the calculation of other physical parameters of the diffuse clouds along these lines of sight.

### 4.1. Reactions

Below are the three reactions which describe the dominant creation and destruction processes for  $\text{H}_3^+$ . Reactions (1) and (2) show the formation process, while reaction (3) shows destruction.



First,  $\text{H}_2$  is ionized to produce  $\text{H}_2^+$  and an electron. This ionization is assumed to be due to a cosmic-ray because Glassgold & Langer (1974) showed that low energy cosmic-rays will penetrate diffuse clouds while the X-ray flux is attenuated in a thin layer at the cloud exterior. They find that for an X-ray with energy 100 eV the optical depth of the cloud

reaches unity at an  $\text{H}_2$  column density of  $2 \times 10^{19} \text{ cm}^{-2}$ . Because most of our sightlines have column densities much larger than this we assume that cosmic-rays are the only ionization mechanism operating throughout the majority of the cloud. After being ionized the  $\text{H}_2^+$  ion reacts with  $\text{H}_2$  to produce  $\text{H}_3^+$  and  $\text{H}$ . The second step is many orders of magnitude faster than the first step (McCall et al. 1998), so the formation rate of  $\text{H}_3^+$  is proportional to the product of the ionization rate and  $\text{H}_2$  density. In diffuse clouds the primary channel of  $\text{H}_3^+$  destruction is electron recombination, which results in either three  $\text{H}$  atoms or one  $\text{H}$  atom and one  $\text{H}_2$  molecule. The destruction rate is given by a rate constant times the product of the number densities of  $\text{H}_3^+$  and electrons.

#### 4.2. Calculations

The steady state approximation assumes that the formation and destruction rates of  $\text{H}_3^+$  are equal. This approximation yields the equation (Geballe et al. 1999)

$$n(\text{H}_2)\zeta_2 = k_e n(\text{H}_3^+)n(e) \quad (4)$$

where  $n(\text{X})$  is the number density of species  $\text{X}$ ,  $\zeta_2$  is the ionization rate of  $\text{H}_2$ , and  $k_e$  is the  $\text{H}_3^+$ -electron recombination rate constant. In contrast to the steady state approximation, time dependent models developed by Liszt (2007) showed that the abundance of  $\text{H}_3^+$  is only weakly dependent on the cosmic-ray ionization rate when a cloud is young. This age is quantified by the ratio of molecular hydrogen to atomic hydrogen  $n(\text{H}_2)/n(\text{H})$  where smaller values correspond to younger clouds. The  $\text{H}_3^+$  abundance becomes weakly dependent on the cosmic-ray ionization rate when  $n(\text{H}_2)/n(\text{H}) \leq 0.05$ . This value corresponds to a molecular hydrogen fraction (defined below in equation (6)) of  $f \leq 0.09$ . Because the  $\text{H}_2$  fractions in all of the clouds we observed are more than double this value, we neglect time dependence and use the steady state approximation.

Assuming that gas is uniformly distributed in the cloud, we can substitute the column density divided by the path length for the number density. By doing this and solving for the ionization rate we obtain

$$\zeta_2 = N(\text{H}_3^+) \frac{k_e}{L} \frac{n(e)}{n(\text{H}_2)}. \quad (5)$$

We further assume that nearly all hydrogen is either in the atomic or molecular state, and define the molecular hydrogen fraction (the fraction of hydrogen nuclei in molecular form) as

$$f \equiv \frac{2n(\text{H}_2)}{n(\text{H}) + 2n(\text{H}_2)} \quad (6)$$

where the denominator is the number density of hydrogen nuclei,  $n_{\text{H}}$ . Solving for  $n(\text{H}_2)$  and plugging the result back into the ionization rate equation we find

$$\zeta_2 = N(\text{H}_3^+) \frac{k_e}{L} \frac{2}{f} \frac{n(e)}{n_{\text{H}}}. \quad (7)$$

In this form it is possible to measure or estimate all of the variables on the right hand side of the equation, so we can derive values for the ionization rate of molecular hydrogen.

The electron recombination rate constant is given by the equation

$$k_e = -1.3 \times 10^{-8} + 1.27 \times 10^{-6} T_e^{-0.48} \text{ (cm}^3 \text{ s}^{-1}\text{)} \quad (8)$$

from McCall et al. (2004) which is valid when the electron temperature,  $T_e$ , is between 10 K and 4000 K. While  $T_e$  is not directly measured, it can be approximated by the excitation temperature derived from the  $J = 0$  and  $J = 1$  levels of molecular hydrogen,  $T_{01}$ . This temperature is calculated from measurements of the column densities of the two levels. In sightlines without these measurements we adopt a value of 60 K. The fact that the observed lines of the  $J = 0$  and  $J = 1$  levels of  $\text{H}_2$  are saturated indicates that few photons are present in the interior of diffuse clouds to radiatively pump these levels. This means that collisions will dominate the equilibrium between these levels. However, the  $J = 0$  and  $J = 1$  levels of  $\text{H}_2$  have different nuclear spin configurations and thus require collisions with species such as  $\text{H}^+$  or  $\text{H}_3^+$  to interconvert (Snow & McCall 2006). If collisions with protons are the dominant factor in determining the relative population of the  $J = 0$  and  $J = 1$  levels though, then  $T_{01}$  should represent the proton kinetic temperature and thus the kinetic temperature of the gas in general (Savage et al. 1977). While electrons produced by photoionization may begin with much higher temperatures, they should thermalize quickly via collisions with  $\text{H}_2$  (McCall et al. 2002). Because  $T_e$  and  $T_{01}$  should both nearly equal the kinetic temperature of the gas, we substitute  $T_{01}$  for  $T_e$  in equation (8).

Assuming that nearly all electrons in diffuse clouds are produced via the ionization of C to  $\text{C}^+$  and that nearly all atomic carbon has been singly ionized (van Dishoeck & Black 1986), the carbon to hydrogen ratio should approximate the electron to hydrogen ratio. Cardelli et al. (1996) found this value to be about  $1.4 \times 10^{-4}$  in multiple diffuse clouds. Because of the relative uniformity of this ratio in all six of their sightlines, we adopt a single average value for use in all of our calculations.

The molecular hydrogen fraction is dependent on H and  $\text{H}_2$  number densities, quantities which surely vary through the cloud, but whose variations are not readily measurable. Because fluctuations in number density cannot be directly measured, we use column densities in place of the number densities in equation (6) and calculate what Snow & McCall (2006) refer to as  $f^N$  in clouds where we have measurements of the H and  $\text{H}_2$  column densities.

However,  $f^N$  is most likely an underestimate of  $f$  in the more molecular regions of the cloud which contain higher concentrations of  $\text{H}_3^+$ . This is because atomic hydrogen is more widely distributed than molecular hydrogen and column densities measure material along the entire line of sight (Snow & McCall 2006). Since the measurement of  $N(\text{H})$  includes material not associated with  $\text{H}_2$ ,  $f^N$  underestimates the  $\text{H}_2$  fraction in the molecular region. For sightlines where measurements are lacking we use  $f = 0.67$ , the value for which the column densities of H and  $\text{H}_2$  are equal.

When possible, estimates of the number density of hydrogen nuclei,  $n_{\text{H}}$ , are adopted from the literature based on various atomic and molecular diagnostics. In eleven of our sightlines Sonnentrucker et al. (2007) used the observed rotational excitation of  $\text{C}_2$  to infer the sum of the H and  $\text{H}_2$  number densities. This was done by comparing models with various temperatures and number densities to the measured column densities of all the excited states and choosing the best fit. For sightlines where the average value of  $f$  is known, they converted  $n(\text{H} + \text{H}_2)$  to  $n_{\text{H}}$ . For sightlines where  $f$  is not known, our adopted value of  $f = 0.67$  is used to perform the conversion. In two additional cases Jura (1975) measured column densities of H and the  $J = 4$  excited level of  $\text{H}_2$ , and with some assumptions estimated the product  $Rn_{\text{H}}$ , where  $R$  is the rate at which  $\text{H}_2$  forms on grains. Adopting a typical value for  $R$  then allowed for the computation of  $n_{\text{H}}$ . In one more sightline (40 Per) Jenkins et al. (1983) estimated the thermal pressure from measurements of the  $J = 0, 1$ , and 2 fine-structure levels of C for a kinetic temperature of 80 K. Using this pressure estimate and the  $\text{H}_2$  temperature ( $T_{01} = 63$  K), we calculate  $n_{\text{H}}$ . Unfortunately, the results obtained for a given sightline by using each of these methods can be significantly different. For example, in the sightline toward  $\zeta$  Oph Sonnentrucker et al. (2007), Jura (1975), and Jenkins et al. (1983) derived values of  $215 \text{ cm}^{-3}$ ,  $90 \text{ cm}^{-3}$ , and  $117 \text{ cm}^{-3}$ , respectively for  $n_{\text{H}}$ . Because of the uncertainties involved with each method and the different final results, the number densities we use are probably uncertain by about a factor of two. For cases where no number density has been determined, a value of  $250 \text{ cm}^{-3}$  is adopted.

Again assuming a uniform distribution of gas in each cloud, we divide the total hydrogen column densities by these number densities to obtain pathlengths:

$$L = \frac{N_{\text{H}}}{n_{\text{H}}} = \frac{N(\text{H}) + 2N(\text{H}_2)}{n_{\text{H}}}. \quad (9)$$

In sightlines where no H and  $\text{H}_2$  column densities have been determined, the total hydrogen column density is estimated from the color excess and the relation  $N_{\text{H}} \approx E(B - V) \times 5.8 \times 10^{21} \text{ cm}^{-2}$  (Bohlin et al. 1978; Rachford et al. 2002). As the pathlength is calculated directly from the hydrogen number density, it is also uncertain by about a factor of two. Using the above relations and approximations, we calculate the ionization rate of molecular hydrogen,  $\zeta_2$ . However, most studies examine the primary cosmic-ray ionization rate per hydrogen

atom,  $\zeta_p$ . While the ionization efficiencies of H and H<sub>2</sub> are dependent on factors such as the helium abundance and ratio of molecular to atomic hydrogen (Dalgarno et al. 1999), we adopt a more simplified approach and use the conversion factor given by Glassgold & Langer (1974):

$$\zeta_2 = 2.3\zeta_p. \quad (10)$$

This conversion stems from the fact that H<sub>2</sub> contains two hydrogen atoms, so the ionization rate is nearly twice as high. Also,  $\zeta_p$  only accounts for the initial (primary) cosmic-ray ionization while  $\zeta_2$  includes ionization from energetic secondary electrons which were created in the first ionization event. With equation (10) we convert our values of  $\zeta_2$  to  $\zeta_p$  so that they can be directly compared to previous observations. The resulting values for the primary cosmic-ray ionization rate and the specific estimates used for each sightline are shown in Table 4. For completeness, we have performed the same analysis for ten sightlines from McCall et al. (2002) and also included the results in Table 4.

With all of the assumptions we have made, it is important to investigate the uncertainties that will propagate to the cosmic-ray ionization rate. Substituting equations (9) and (10) into equation (7) gives the primary cosmic-ray ionization rate as

$$\zeta_p = \frac{2}{2.3} N(\text{H}_3^+) \frac{n_{\text{H}}}{f} \frac{k_e}{N_{\text{H}}} \left[ \frac{n(e)}{n_{\text{H}}} \right]. \quad (11)$$

In this equation, the molecular hydrogen fraction,  $f$ , and the number density of hydrogen nuclei,  $n_{\text{H}}$ , are the two most uncertain parameters (note that the  $n_{\text{H}}$  in the denominator is part of the ratio  $n(e)/n_{\text{H}}$  which is well determined). Because  $\zeta_p$  is directly proportional to  $n_{\text{H}}$ , any increase or decrease in  $n_{\text{H}}$  produces a corresponding increase or decrease in  $\zeta_p$ . As previously mentioned, the uncertainty in  $n_{\text{H}}$  is probably about a factor of 2. On the other hand,  $\zeta_p$  is inversely related to  $f$ . The H<sub>2</sub> fraction is by definition between zero and one, and most of our measured values are around 0.5. For sightlines with the adopted value of 0.67, the maximum increase is a factor of 1.5. We take this factor to be an approximation for the uncertainty in  $f$ . Because  $f^N$  should always be an underestimate of  $f$  in measured sightlines, we only consider increasing the molecular hydrogen fraction for those sightlines. Taking into account the uncertainties in both  $n_{\text{H}}$  and  $f$ , the true value of  $\zeta_p$  in sightlines with measurements of  $f^N$  is likely between one third and twice our derived estimate of  $\zeta_p$ . For sightlines with no measured H<sub>2</sub> fraction, we allow  $f$  to vary both up or down by a factor of 1.5. This results in a possible cosmic-ray ionization rate between  $\zeta_p/3$  and  $3\zeta_p$ . These limits arise when the most extreme variations in both  $f$  and  $n_{\text{H}}$  are substituted into equation (11). However,  $f$  tends to be higher when  $n_{\text{H}}$  is higher because the rate of H<sub>2</sub> formation scales as the square of  $n_{\text{H}}$ . This suggests that it is probable that  $f$  and  $n_{\text{H}}$  will vary in the same way,

so that the above analysis most likely overestimates the range of possible ionization rates.

### 4.3. $\text{H}_3^+$ Temperature

Another property of the gas to be examined is the excitation temperature, determined from relative populations of the different rotational states of  $\text{H}_3^+$ . For the two lines we have observed the temperature may be determined from the equation

$$\frac{N_{ortho}}{N_{para}} = \frac{g_{ortho}}{g_{para}} e^{-\Delta E/kT} = 2e^{-32.87/T} \quad (12)$$

taken from McCall et al. (1998). In this case *ortho* refers to the population of the (1,0) state and *para* to the (1,1) state. The  $g$ 's are statistical weights,  $\Delta E$  is the energy difference between the states,  $k$  is the Boltzmann constant, and  $T$  is the temperature. Excitation temperatures derived from this equation are shown in Table 4.

If the rotational (de-)excitation of  $\text{H}_3^+$  is dominated by collisions with  $\text{H}_2$ , then the temperature measurements from both species should be similar. However, this is not the case. Most  $\text{H}_2$  temperatures are around 60 K while the  $\text{H}_3^+$  temperatures are typically about 30 K. This same discrepancy was described by McCall et al. (2003). In their model calculation of  $\text{H}_3^+$  thermalization, Oka & Epp (2004) have shown that the (1,1)/(1,0) excitation temperature is always lower than the  $\text{H}_2$  temperature because of cooling by fast spontaneous emission from the (2,2) to (1,1) state. For the typical cloud conditions in this paper ( $n_{\text{H}} \sim 250 \text{ cm}^{-3}$ ,  $T \sim 60 \text{ K}$ ) the model of Oka & Epp (2004) produces an  $\text{H}_3^+$  excitation temperature of about 50-55 K which is significantly higher than the observed values of about 30 K. The source of this discrepancy remains unclear.

## 5. Discussion

### 5.1. Inferred Ionization Rates

Values of the cosmic-ray ionization rate for diffuse clouds observed here as well as those determined for other diffuse clouds observed previously by us are given in the right hand column of Table 4. The detected values in the lines of sight to fourteen sources cover the range  $0.5\text{--}3.2 \times 10^{16} \text{ s}^{-1}$ . Upper limits, which are given for fifteen diffuse clouds, are consistent with this range of ionization rates, with the possible exception of HD 168607. While most of the detections of  $\text{H}_3^+$  are confined to the Galactic plane, they are widely dispersed in Galactic longitude. We therefore conclude that the values of the cosmic-ray ionization rate listed in

Table 4 are typical for Galactic diffuse interstellar clouds.

A few of the sightlines we investigated have been studied previously to derive cosmic-ray ionization rates. All of these studies used column densities of either OH, HD, or both in their calculations. Because the formation pathways of OH and HD include the ionization of atomic hydrogen, they can be used to determine the H ionization rate. Most of these studies (Black & Dalgarno 1977; Black et al. 1978; Hartquist et al. 1978a; Federman et al. 1996) then derived the primary cosmic-ray ionization rate from the H ionization rate, but O'Donnell & Watson (1974) did not because they still considered ionization via X-rays to be important. Our values of the primary ionization rate for  $\zeta$  Per,  $\sigma$  Per,  $\epsilon$  Per,  $\xi$  Per, and  $\zeta$  Oph are shown in Table 5 along with the rates derived from OH and HD measurements as well as cloud modeling. For  $\zeta$  Per our value is over an order of magnitude larger than those reported by Hartquist et al. (1978b) and Federman et al. (1996). While the rest of our new measurements in Table 5 are only upper limits, these are also typically orders of magnitude larger than previously published values. The only exception is  $\sigma$  Per where both papers cite values of  $\zeta_p$  about one fourth to one half our upper limit.

Various model calculations were performed by van Dishoeck & Black (1986) to investigate three of the sightlines that we study here:  $\zeta$  Oph,  $\zeta$  Per, and  $\sigma$  Per. In creating these models they used the most recent measurements of rate constants and the column densities of diagnostic species such as H and H<sub>2</sub> as input parameters. By varying a few uncertain parameters, they would then generate lists of predicted column densities for many atomic and molecular species under slightly different conditions. When their paper was written, it was believed that the H<sub>3</sub><sup>+</sup>-electron recombination rate constant was much lower than the currently accepted value. Smith & Adams (1984) reported an upper limit corresponding to 10<sup>-7</sup> cm<sup>3</sup> s<sup>-1</sup> at  $T = 40$  K, and Adams & Smith (1987) lowered the upper limit to 10<sup>-11</sup> cm<sup>3</sup> s<sup>-1</sup> at  $T = 80$  K. Due to the wide range of possible recombination rate constants, van Dishoeck & Black (1986) performed calculations using both 10<sup>-7</sup> and 10<sup>-10</sup> cm<sup>3</sup> s<sup>-1</sup>. The cosmic-ray ionization rates from their paper listed in Table 5 were computed by determining  $\zeta_p$  necessary to reproduce observed OH column densities when  $k_e = 10^{-7}$  cm<sup>3</sup> s<sup>-1</sup>. We choose to compare these ionization rates to ours because we obtain  $k_e = 1.6 \times 10^{-7}$  cm<sup>3</sup> s<sup>-1</sup> when  $T = 60$  K is used as the input temperature in equation (8). The value of  $\zeta_p$  inferred by van Dishoeck & Black (1986) is about the same as ours for  $\zeta$  Per, but the lower limits they derived for  $\zeta$  Oph and  $\sigma$  Per are larger than our upper limits for both of those sightlines.

For their models that used  $k_e = 10^{-10}$  cm<sup>3</sup> s<sup>-1</sup>, van Dishoeck & Black (1986) obtained cosmic-ray ionization rates that are about a factor of 1 to 5 times smaller than ours. From these models they also predicted the column density of H<sub>3</sub><sup>+</sup> along each sightline. Their results

are all on the order of  $N(\text{H}_3^+) \sim 10^{14} \text{ cm}^{-2}$ , which is a few times larger than the observed column densities or upper limits in any of these sightlines. Because van Dishoeck & Black (1986) use only a slightly smaller cosmic-ray ionization rate (corresponding to the formation rate) but a much smaller recombination rate (corresponding to the destruction rate), their prediction of an  $\text{H}_3^+$  column density similar to observed values seems somewhat serendipitous. In addition to the overestimate of the  $\text{H}_3^+$  column density, a small  $\text{H}_3^+$ -electron recombination rate constant may have further consequences. Dalgarno (2006) noted that a small value of  $k_e$  may have been responsible for underestimates of the primary cosmic-ray ionization rate in the past. This is because a slower destruction rate requires a slower formation rate to produce a given abundance.

In addition to the slow recombination rate, there are some other possible explanations for differences between the cosmic-ray ionization rate inferred from  $\text{H}_3^+$  and those inferred from OH and HD. Le Petit et al. (2004) pointed out that the rate constant associated with the endothermic charge transfer from  $\text{H}^+$  to O varies over the temperatures typically associated with diffuse clouds. This means that the OH production rate is temperature dependent. The ionization rates towards  $\zeta$  Per and  $\zeta$  Oph quoted in Hartquist et al. (1978b) were derived using temperatures of 120 K and 110 K, respectively, for the warm components of the cloud models along each sightline (Black et al. 1978; Black & Dalgarno 1977). As these temperatures are about twice as large as the values determined from  $\text{H}_2$ , their OH production is much more efficient. The result is a smaller cosmic-ray ionization rate needed to produce the observed OH column density than if a lower temperature had been used. This problem was addressed by the later models of van Dishoeck & Black (1986) where tempertaure and density were varied as functions of cloud depth.

Le Petit et al. (2004) went on to make a comprehensive chemical model of the cloud towards  $\zeta$  Per. They determined the value of  $\zeta_p$  that would best reproduce all observed atomic and molecular column densities to be  $2.5 \times 10^{-16} \text{ s}^{-1}$ , which is in good agreement with our estimate of  $3.2 \times 10^{-16} \text{ s}^{-1}$ . The difference in these values may arise because we assume a uniform distribution of gas while Le Petit et al. (2004) invoke a three phase model which includes diffuse gas, dense gas, and magnetohydrodynamic shocks.

Two different effects may lead to underestimates of  $\zeta_p$  from measurements of HD. The first has to do with an overestimate of the total deuterium to hydrogen ratio  $n_{\text{D}}/n_{\text{H}}$ . This ratio can be used to estimate the molecular deuterium fraction,  $N(\text{HD})/N(\text{H}_2)$ . However, the observed values of  $N(\text{HD})/N(\text{H}_2)$  are about an order of magnitude smaller than those predicted by  $n_{\text{D}}/n_{\text{H}}$ . To explain this discrepancy, Liszt (2006) argued that the atomic deuterium fraction must be larger than the total deuterium fraction. This means that approximating  $n_{\text{D}}/n_{\text{H}}$  with  $N(\text{D})/N(\text{H})$  overestimates the total deuterium to hydrogen ratio.

Federman et al. (1996) showed that the cosmic-ray ionization rate is inversely related to the deuterium fraction, so an overestimate of  $n_{\text{D}}/n_{\text{H}}$  will underestimate  $\zeta_p$ .

Secondly, Liszt (2003) emphasized the importance of grain neutralization proposed by Lepp et al. (1988). This process reduces the number of  $\text{H}^+$  ions in the gas through charge transfer with small grains. By lowering the abundance of  $\text{H}^+$ , the production rate of HD will decrease. This is because HD formation is dependent upon the reaction involving the charge transfer from  $\text{H}^+$  to D. Since neutralization slows down HD production, a larger value of  $\zeta_p$  is needed to create a given abundance than if the effect were not taken into account. Liszt (2003) used a model which includes grain neutralization and showed that both  $\text{H}_3^+$  and HD column densities can be reproduced with a single ionization rate of  $\zeta_p \geq 2 \times 10^{-16} \text{ s}^{-1}$ . Since OH formation is dependent on a similar charge transfer reaction, grain neutralization and thus a larger cosmic-ray ionization rate may be necessary in its analysis as well.

McCall et al. (2003) studied  $\text{H}_3^+$  in the sightline towards  $\zeta$  Per. Using nearly the same analysis as this paper, they inferred a value of  $\zeta_2 = 1.2 \times 10^{-15} \text{ s}^{-1}$  which is equivalent to  $\zeta_p = 5.2 \times 10^{-16} \text{ s}^{-1}$  shown in Table 5. This higher ionization rate is due to various differences in input parameters. In terms of the parameters in this paper, McCall et al. (2003) used  $1.5k_e$ ,  $1.2N(\text{H}_3^+)$ ,  $1.2n_{\text{H}}$ , and  $0.8n(e)/n_{\text{H}}$  for the following reasons. The  $\text{H}_3^+$ -electron recombination rate constant differs because they approximated the electron temperature with the  $\text{H}_3^+$  temperature instead of the  $\text{H}_2$  temperature in equation (8). Further observations have more than doubled the total integration time so that the spectrum and  $\text{H}_3^+$  column density change slightly between papers. The value of  $n_{\text{H}}$  used by McCall et al. (2003) was an average number density computed from various measurements, whereas the value used in this paper comes from the  $\text{C}_2$  analysis of Sonnentrucker et al. (2007). Finally, we have adopted a single value of  $n(e)/n_{\text{H}}$  to be used in all calculations while they used  $\text{H}_2$  and  $\text{C}^+$  column densities measured towards  $\zeta$  Per.

While all of the observations and models above are viable methods for finding the cosmic-ray ionization rate, we believe that the use of  $\text{H}_3^+$  should produce the best results due to its relatively simple chemistry. Using either OH or HD to calculate  $\zeta_p$  requires more measurements, more assumptions, and more variable parameters than using  $\text{H}_3^+$ . More parameters give the opportunity for a greater uncertainty to accumulate during the calculation. Fewer uncertainties coupled with advances in instrumentation lead us to speculate that the cosmic-ray ionization rates inferred from  $\text{H}_3^+$  may be the most accurate to date for diffuse clouds. However, improved estimates of  $f$  and  $n_{\text{H}}$ , the two most uncertain values in our calculations, would make  $\text{H}_3^+$  an even better probe of the cosmic-ray ionization rate.

## 5.2. Theoretical Ionization Rates

Several theoretical calculations of  $\zeta_p$  have been performed in the last half-century (Hayakawa et al. 1961; Spitzer & Tomasko 1968; Nath & Biermann 1994; Webber 1998). In these papers the authors derived a cosmic-ray ionization rate starting from the observed flux of cosmic-rays in our solar system. Unfortunately, there are large uncertainties associated with this method. The cosmic-ray spectrum is well measured above about 1 GeV, but lower energy particles are deflected from the inner solar system by the magnetic field coupled to the solar wind. The particles which are most important for ionizing species in diffuse clouds are likely those with energies from about 2 to 10 MeV. Since this portion of the spectrum cannot be directly measured, the flux at low energies must somehow be extrapolated from existing data. Hayakawa et al. (1961) assumed that the power law which applies to the flux of high energy cosmic-rays continues down to 10 MeV where the spectrum peaks and then decreases linearly with energy. From these assumptions they derived an ionization rate of  $10^{-15} \text{ s}^{-1}$ . Spitzer & Tomasko (1968), however, fit a curve to measurements of cosmic-rays with energies near 100 MeV that also matches the high energy spectrum power law. With this method, their spectrum peaks around 100 MeV and falls off for lower energies. The result of using their fit is a lower limit of  $6.8 \times 10^{-18} \text{ s}^{-1}$ . In the same paper they derived an upper limit of  $1.2 \times 10^{-15} \text{ s}^{-1}$  via arguments that low energy cosmic-ray protons are accelerated in Type I supernova shells. Webber (1998) used data from the *Pioneer* and *Voyager* spacecraft as they travelled outward in the solar system where the weaker solar wind allows for the detection of lower-energy cosmic-rays. These data were then combined with previous observations to infer the interstellar proton spectrum. Using this proton spectrum and a heavy nuclei spectrum both with low energy cut-offs at 10 MeV and an electron spectrum cut-off below 2 MeV, Webber (1998) calculated the primary cosmic-ray ionization rate to be  $(3-4) \times 10^{-17} \text{ s}^{-1}$ . Our ionization rates fall neatly within the bounds formed by these studies and so are not inconsistent with constraints based on direct cosmic-ray measurements and theoretical particle physics.

## 5.3. The Ionization Rate in Dense Clouds

In contrast to our findings in diffuse clouds, the cosmic-ray ionization rate in dense clouds does seem to agree with the canonical value. Observations of  $\text{H}_3^+$  towards dense clouds have found column densities roughly the same as those seen in diffuse clouds (Geballe & Oka 1996; McCall et al. 1999). These measurements have been used to calculate the product  $\zeta_2 L$ . When  $\zeta_2$  is taken to be the canonical value of  $\sim 3 \times 10^{-17} \text{ s}^{-1}$ , the resulting pathlength is on the order of a parsec. This is a typical size for dense clouds as measured by other methods

such as extinction mapping. Since  $\text{H}_3^+$  should be a reliable tracer for the cosmic-ray ionization rate in both environments, there must be some mechanism causing the difference between dense and diffuse clouds. One possibility examined by both Skilling & Strong (1976) and Padoan & Scalo (2005) is cosmic-ray self-confinement. In this process cosmic-rays generate Alfvén waves which can effectively confine the lower energy particles ( $\lesssim 100$  MeV) to diffuse material, thus preventing them from entering dense clouds. Because cosmic-rays in the 1–100 MeV range are the most efficient at ionization, self-confinement naturally leads to a higher ionization rate in diffuse clouds than in dense clouds. Another possibility is that there is a previously unrecognized high flux of low energy cosmic-rays that can penetrate diffuse but not dense clouds. Assuming that typical column densities of diffuse clouds are of order  $10^{21} \text{ cm}^{-2}$  and those of dense clouds are of order  $10^{23} \text{ cm}^{-2}$ , cosmic-rays with energies  $\sim 2\text{--}20$  MeV (Cravens & Dalgarno 1978) would contribute to the ionization rate only in diffuse clouds. As we foresee no observational techniques that would distinguish between these two possibilities, a resolution to this question will depend on more sophisticated theoretical treatments.

## 6. SUMMARY & CONCLUSIONS

We have surveyed twenty sightlines and detected  $\text{H}_3^+$  along eight of them. Column densities are measured for these eight sightlines, and upper limits set for the remaining twelve. Besides a concentration near the Galactic plane, there seems to be no clear correlation between location in the sky and detecting  $\text{H}_3^+$ , so it is unlikely that we are observing anomalous regions in the Galaxy. Instead, finding  $\text{H}_3^+$  in so many sightlines suggests that it is ubiquitous in the diffuse ISM.

From the  $\text{H}_3^+$  column densities and the steady state approximation, we derive cosmic-ray ionization rates for the nineteen diffuse cloud sightlines in this study along with ten sightlines from McCall et al. (2002). Typical values are on the order of  $\zeta_p \approx 2 \times 10^{-16} \text{ s}^{-1}$ , which falls within theoretical constraints. While this is an order of magnitude larger than most previously inferred values, there are several possible explanations for the discrepancy. The most likely candidates are rate constants with uncertain measurements and physical or chemical effects not included in past models. Newer models that do take into account these factors require cosmic-ray ionization rates very similar to our inferred values. Coupled with these models, our widespread detection of  $\text{H}_3^+$  in diffuse clouds supports the idea that the typical cosmic-ray ionization rate in such regions should be revised upward by about an order of magnitude.

The authors would like to thank J. H. Black and H. S. Liszt for helpful comments and suggestions, and acknowledge the staff of UKIRT and the developers of the data reduction packages used in this paper. The United Kingdom Infrared Telescope is operated by the Joint Astronomy Centre on behalf of the U.K. Particle Physics and Astronomy Research Council. The ORAC-DR and FIGARO software packages were provided by the Starlink Project which is run by CCLRC on behalf of PPARC. NI and BJM have been supported by NSF grant PHY 05-55486. TO has been supported by NSF grant PHY 03-54200. TRG’s research is supported by the Gemini Observatory, which is operated by the Association of Universities for Research in Astronomy, Inc., on behalf of the international Gemini partnership of Argentina, Australia, Brazil, Canada, Chile, the United Kingdom, and the United States of America.

## REFERENCES

Adams, N. G., & Smith, D. 1987, in IAU Symposium 120, Astrochemistry, ed. M. S. Vardya & S. P. Tarafdar (Dordrecht: Reidel), 1

Black, J. H., & Dalgarno, A. 1977, ApJS, 34, 405

Black, J. H., Hartquist, T. W., & Dalgarno, A. 1978, ApJ, 224, 448

Bohlin, R. C., Savage, B. D., & Drake, J. F. 1978, ApJ, 224, 132

Cardelli, J. A., Meyer, D. M., Jura, M., & Savage, B. D. 1996, ApJ, 467, 334

Chaffee, F. H., Jr., & White, R. E. 1982, ApJS, 50, 169

Cravens, T. E., & Dalgarno, A. 1978, ApJ, 219, 750

Crutcher, R. M., & Chu, Y. H. 1982, in Regions of Recent Star Formation, ed. R. S. Roger & P. E. Dewdney (Dordrecht: Reidel), 53

Dalgarno, A., Yan, M., & Liu, W. 1999, ApJS, 125, 237

Dalgarno, A. 2006, PNAS, 103, 12269

Federman, S. R., & Lambert, D. L. 1992, AJ, 104, 691

Federman, S. R., Weber, J., & Lambert, D. L. 1996, ApJ, 463, 181

Geballe, T. R., McCall, B. J., Hinkle, K. H., & Oka, T. 1999, ApJ, 510, 251

Geballe, T. R., & Oka, T. 1996, Nature, 384, 334

Glassgold, A. E., & Langer, W. D. 1974, *ApJ*, 193, 73

Gredel, R., & Münch, G. 1986, *A&A*, 154, 336

Hartquist, T. W., Black, J. H., & Dalgarno, A. 1978a, *MNRAS*, 185, 643

Hartquist, T. W., Doyle, H. T., & Dalgarno, A. 1978b, *A&A*, 68, 65

Hayakawa, S., Nishimura, S., & Takayanagi, T. 1961, *PASJ*, 13, 184

Hobbs, L. M., Thorburn, J. A., Oka, T., Barentine, J., Snow, T. P., & York, D. G. 2004, *ApJ*, 615, 947

Jura, M. 1975, *ApJ*, 197, 581

Jenkins, E. B., Jura, M., & Loewenstein, M. 1983, *ApJ*, 270, 88

Lamers, H. J. G. L. M., de Groot, M., & Cassatella, A. 1983, *A&A*, 128, 299

Le Petit, F., Roueff, E., & Herbst, E. 2004, *A&A*, 417, 993

Lepp, S., Dalgarno, A., van Dishoeck, E. F., & Black, J. H. 1988, *ApJ*, 329, 418

Liszt, H. 2003, *A&A*, 398, 621

Liszt, H. S. 2006, *A&A*, 452, 269

Liszt, H. S. 2007, *A&A*, 461, 205

McCall, B. J. 2000, *Philos. Trans. R. Soc. London A*, 358, 2385

McCall, B. J. 2001, Ph.D. thesis, Univ. Chicago

McCall, B. J., Geballe, T. R., Hinkle, K. H., & Oka, T. 1998, *Science*, 279, 1910

McCall, B. J., Geballe, T. R., Hinkle, K. H., & Oka, T. 1999, *ApJ*, 522, 338

McCall, B. J., & Oka, T. 2000, *J. Chem. Phys.*, 113, 3104

McCall, B. J., et al. 2002, *ApJ*, 567, 391

McCall, B. J., et al. 2003, *Nature*, 422, 500

McCall, B. J., et al. 2004, *Phys. Rev. A*, 70, 052716

Mountain, C. M., Robertson, D. J., Lee, T. J., & Wade, R. 1990, *Proc. SPIE*, 1235, 25

Nath, B. B., & Biermann, P. L. 1994, MNRAS, 267, 447

O'Donnell, E. J., & Watson, W. D. 1974, ApJ, 191, 89

Oká, T., & Epp, E. 2004, ApJ, 613, 349

Padoan, P., & Scalo, J. 2005, ApJ, 624, L97

Pendleton, Y. J., Sandford, S. A., Allamandola, L. J., Tielens, A. G. G. M., & Sellgren, K. 1994, ApJ, 437, 683

Rachford, B. L. et al. 2002, ApJ, 577, 221

Rickard, J. J. 1974, A&A, 31, 47

Savage, B. D., Bohlin, R. C., Drake, J. F., & Budich, W. 1977, ApJ, 216, 291

Schulte, D. H. 1958, ApJ, 128, 41

Shuping, R. Y., Snow, T. P., Crutcher, R., & Lutz, B. L. 1999, ApJ, 520, 149

Skilling, J., & Strong, A. W. 1976, A&A, 53, 253

Smith, D., & Adams, N. G. 1984, ApJ, 284, L13

Snow, T. P., & McCall, B. J. 2006, ARA&A, 44, 367

Snow, T. P., Jr., York, D. G., & Welty, D. E. 1977, AJ, 82, 113

Sonnentrucker, P., Welty, D. E., Thorburn, J. A., & York, D. G. 2007, ApJS, 168, 58

Spitzer, L., Jr., & Tomasko, M. G. 1968, ApJ, 152, 971

Thorburn, J. A., et al. 2003, ApJ, 584, 339

van Dishoeck, E. F., & Black, J. H. 1986, ApJS, 62, 109

Webber, W. R. 1998, ApJ, 506, 329

Wegner, W. 1994, MNRAS, 270, 229

Welty, D. E., & Hobbs, L. M. 2001, ApJS, 133, 345

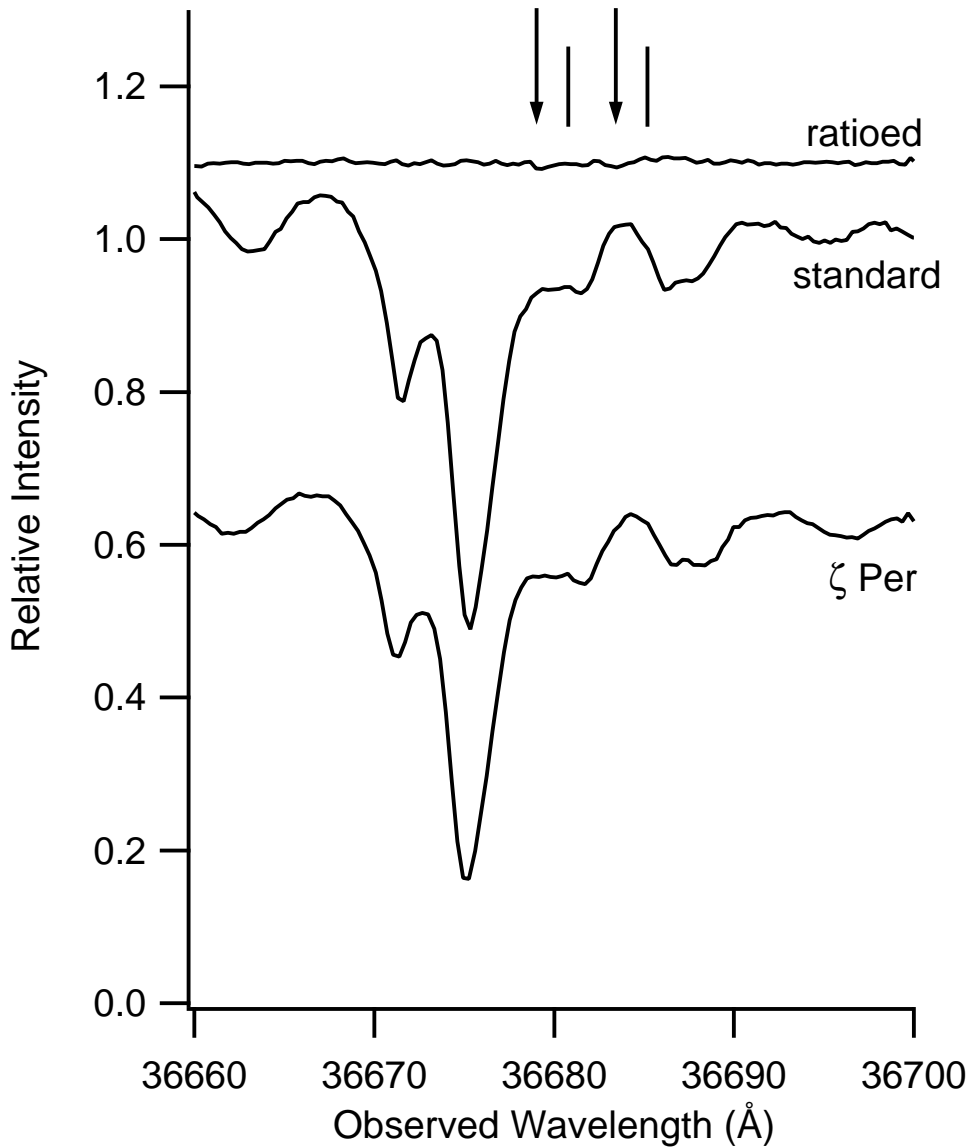


Fig. 1.— Typical examples of spectra near the  $\text{H}_3^+$  ortho-para doublet. The spectra in this and all other figures have been offset in intensity for clarity. The bottom spectrum is  $\zeta$  Per from 2001 September 5. The middle spectrum is the standard star  $\beta$  Per from the same date. The top spectrum is  $\zeta$  Per ratioed with the standard star. Two arrows show the expected location of  $\text{H}_3^+$  absorption which can barely be seen here due to the scaling. The vertical lines are at the rest wavelengths of the  $\text{H}_3^+$  lines.

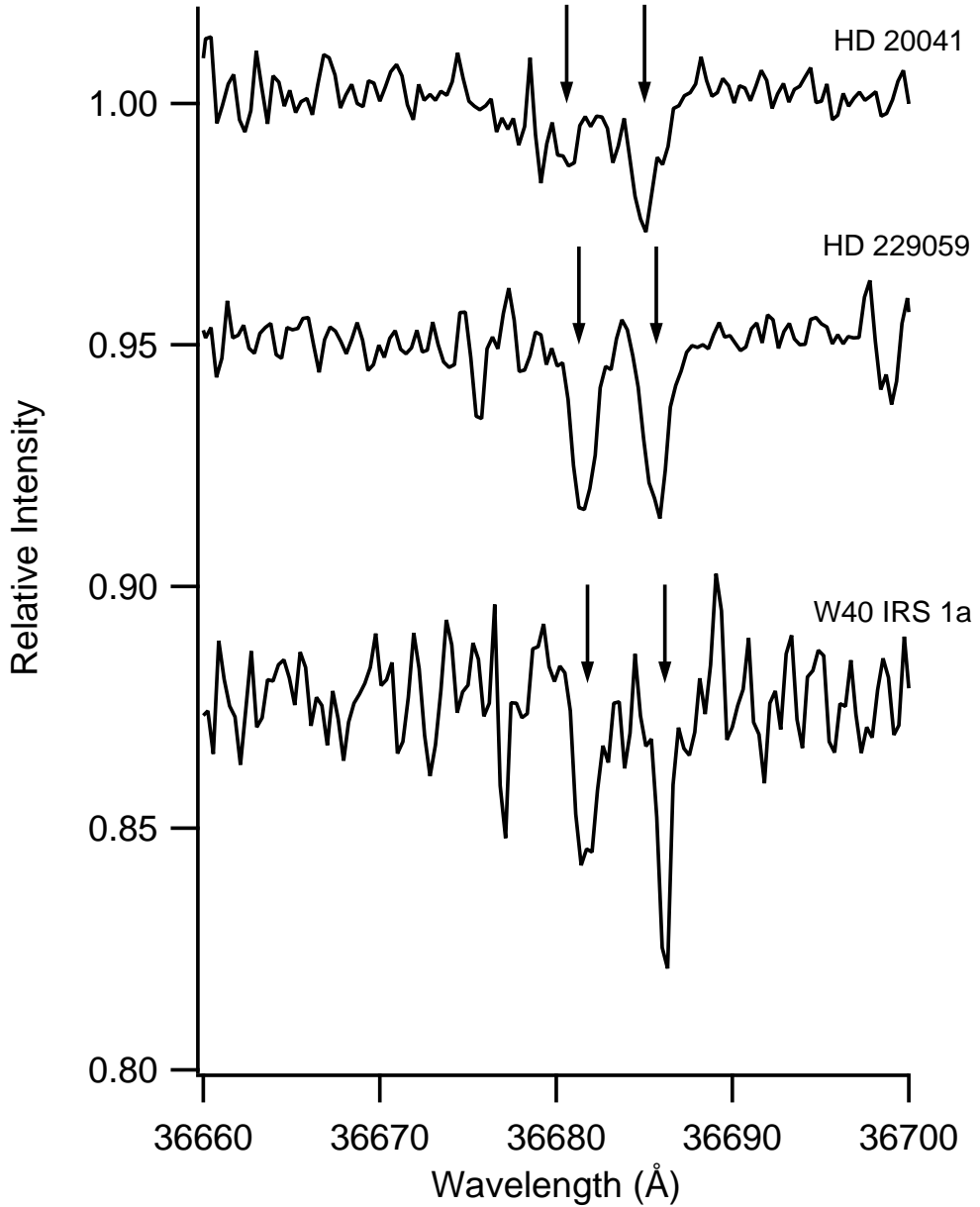


Fig. 2.— Spectra showing strong detections of the H<sub>3</sub><sup>+</sup> doublet near 36680 Å. All spectra have been Doppler shifted into the rest frame of the LSR. Arrows show where the lines are expected due to previous gas velocity measurements, which are given in Table 2.

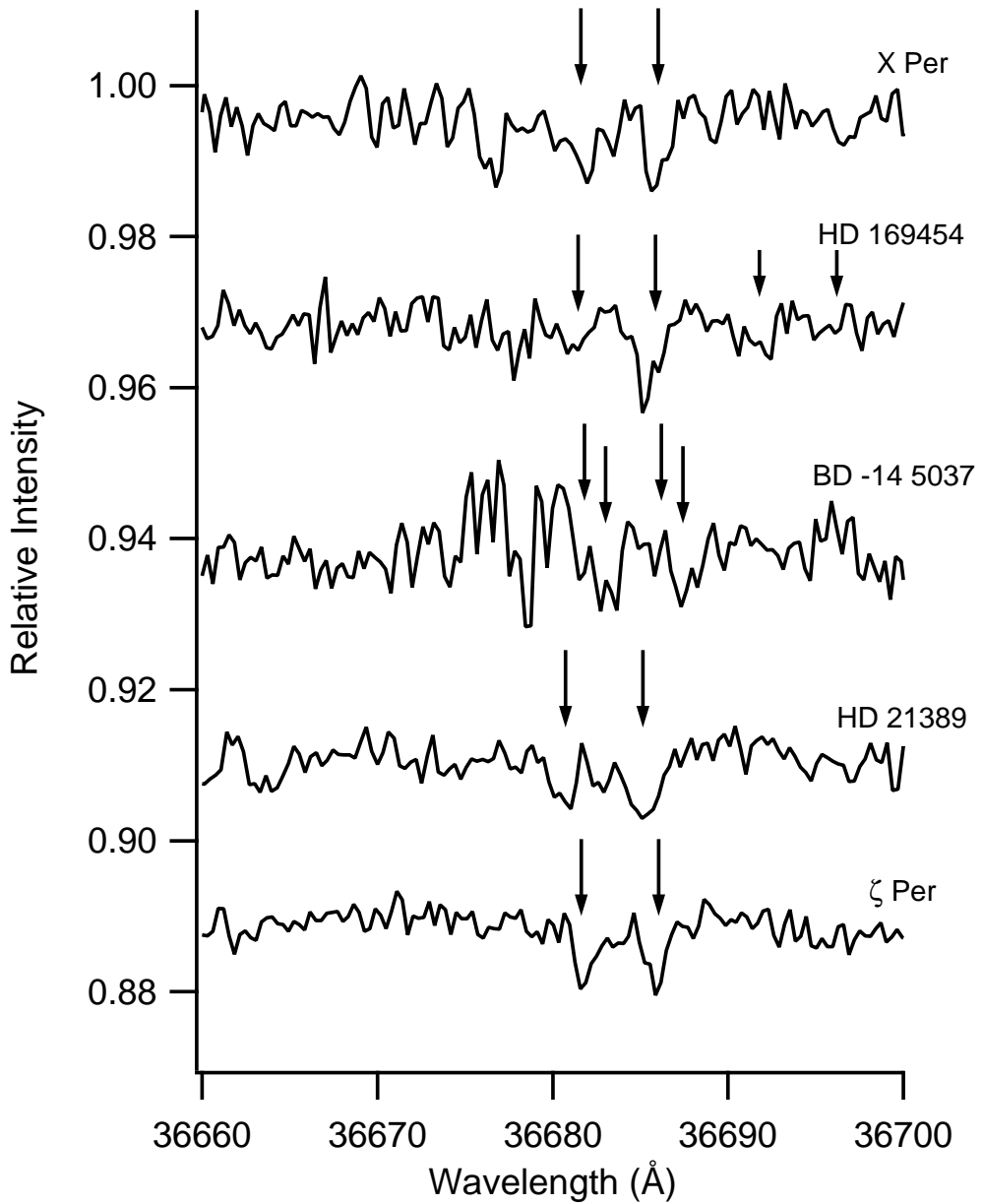


Fig. 3.— Same as Figure 2 except showing more typical strength detections of  $\text{H}_3^+$ .

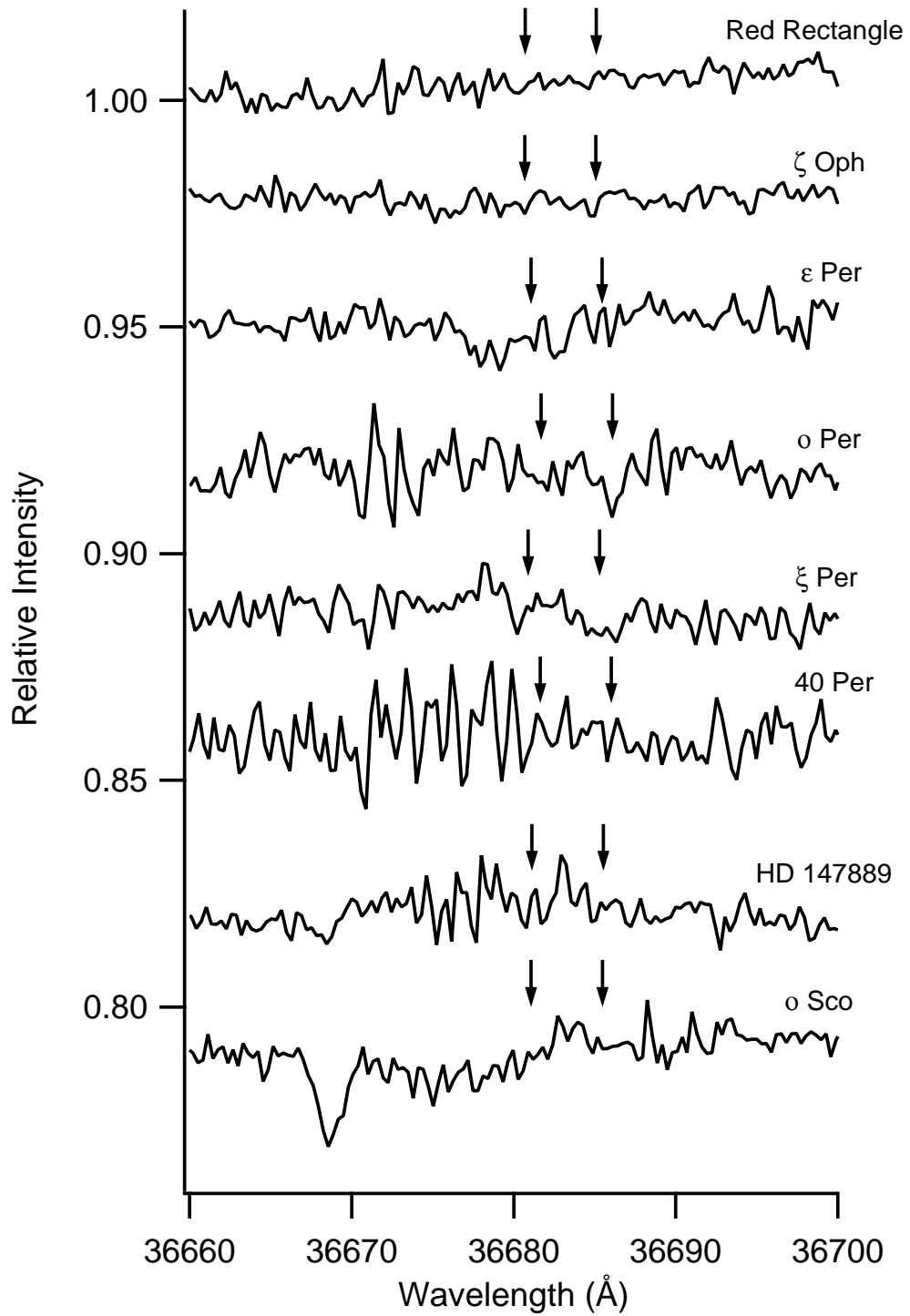


Fig. 4.— Same as Figure 2 except showing non-detections.

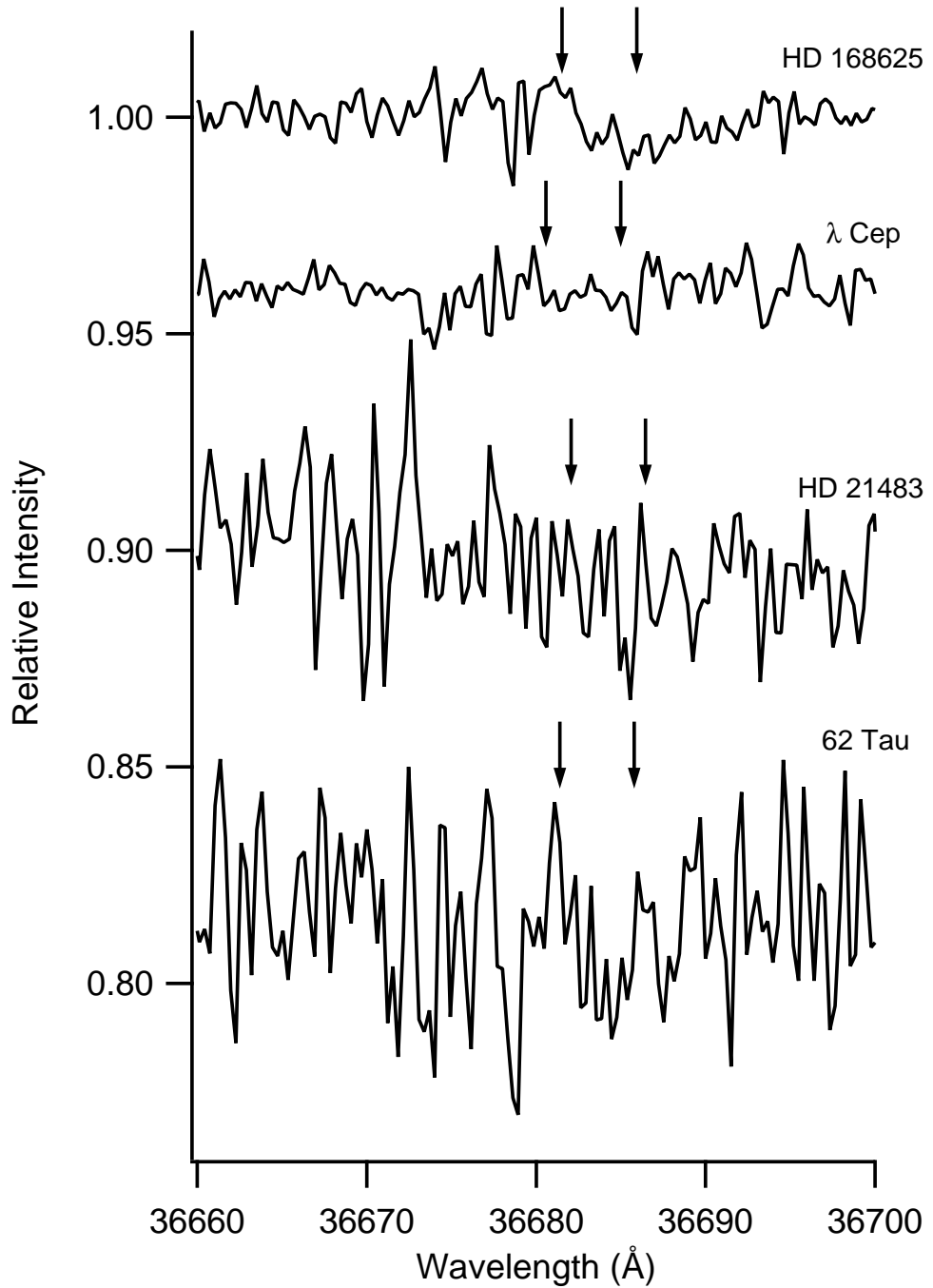


Fig. 5.— Same as Figure 2 except showing non-detections.

Table 1. Observations

Object	HD number	Date(s) of Observation	Standard	Integration Time (sec)
$\zeta$ Oph	149757	2001 May 24	$\beta$ Lib	576
		2001 May 25	$\beta$ Lib	1344
HD 147889	147889	2001 May 24	$\delta$ Sco	5760
$\lambda$ Cep	210839	2001 May 24	$\alpha$ Lyr	4320
HD 169454	169454	2001 May 25	$\beta$ Lib	4224
W40 IRS 1a	...	2001 May 25	$\eta$ Oph	1800
		2001 May 26	$\delta$ Sco	1800
$\sigma$ Sco	147084	2001 May 26	$\alpha$ Lyr	960
HD 168625	168625	2001 May 26	$\eta$ Oph	1440
HD 229059	229059	2001 May 27	$\alpha$ Cyg	1800
		2001 Sept 5	$\alpha$ Cyg	1800
BD -14 5037	...	2001 May 28	$\eta$ Oph	2016
HD 20041	20041	2001 Sept 5	$\beta$ Per	1728
HD 21389	21389	2001 Sept 5	$\beta$ Per	1536
		2002 Dec 30	$\delta$ Per	1152
		2002 Dec 31	$\beta$ Per	1536
		2003 Jan 1	$\eta$ Tau	1152
$\zeta$ Per	24398	2001 Sept 5	$\beta$ Per	2304
		2002 Dec 30	$\beta$ Per	1152
		2002 Dec 31	$\beta$ Per	1152
		2003 Jan 1	$\delta$ Per	1440
$\sigma$ Per	23180	2002 Dec 30	$\beta$ Per	2304
		2002 Dec 31	$\beta$ Per	1152
$\xi$ Per	24912	2002 Dec 30	$\beta$ Per	1920
		2002 Dec 31	$\beta$ Per	1920
		2003 Jan 1	$\delta$ Per	1536
		2005 Jan 6	$\eta$ Aur	2880
X Per	24534	2002 Dec 31	$\beta$ Per	1920
		2004 Jan 22	HD 17573	3600
		2005 Jan 5	HD 17573	4320
		2005 Jan 6	$\eta$ Aur	2880

Table 1—Continued

Object	HD number	Date(s) of Observation	Standard	Integration Time (sec)
62 Tau	27778	2005 Mar 3	$\eta$ Aur	5040
		2005 Mar 4	$\eta$ Aur	5040
$\epsilon$ Per	24760	2003 Jan 1	$\beta$ Per	2688
$\epsilon$ Per	24760	2004 Jan 23	$\eta$ Aur	1800
		2005 Jan 5	$\eta$ Aur	1440
40 Per	22951	2005 Jan 6	$\eta$ Aur	1440
		2004 Jan 23	HD 17573	3600
Red Rectangle	44179	2005 Jan 6	$\eta$ Aur	2880
		2005 Jan 6	$\kappa$ Ori	720
HD 21483	21483	2005 Jan 25	HD 17573	5760

Table 2. Previous Measurements of ISM Gas Velocities

Object	$v_{\text{LSR}}$ (km s $^{-1}$ )	Species	Reference
HD 20041	-1.6	K I	1
HD 21389	-0.5	CH	1
$\zeta$ Per	6.9	CH	1
X Per	6.6	CH	1
HD 169454	5.3	CH	1
	90	Na I & Ca II	2
HD 229059	4.04	K I	3
BD -14 5037	8.2	C <sub>2</sub>	4
	18.2	C <sub>2</sub>	4
W40 IRS 1a	8	<sup>13</sup> CO $^{\dagger}$	5
HD 21483	10.3	CH	1
40 Per	6.8	K I	3
$\sigma$ Per	7.3	CH	1
$\epsilon$ Per	2.2	K I	6
$\xi$ Per	0.55	K I	6
62 Tau	4.8	CH	1
Red Rectangle	-0.8	K I $^{\dagger}$ & O I $^{\dagger}$	7
$\sigma$ Sco	2.29	K I	6
HD 147889	2.7	K I	1
$\zeta$ Oph	-1.0	CH	1
HD 168625	6	Ca II	8
$\lambda$ Cep	-1.7	CH	1

References. — (1) Welty (private communication); (2) Federman & Lambert (1992); (3) Chaffee & White (1982); (4) Gredel & Münch (1986); (5) Crutcher & Chu (1982); (6)

Welty & Hobbs (2001); (7) Hobbs et al. (2004); (8) Rickard (1974)

Note. —  $v_{\text{LSR}}$  is the velocity of the interstellar gas in the local standard of rest frame. Unless noted, all lines were measured in absorption.

<sup>†</sup>measured in emission

Table 3. Absorption Line Parameters

Object	Transition	$v_{\text{LSR}}$ (km s $^{-1}$ )	FWHM (km s $^{-1}$ )	$W_\lambda$ (Å)	$\sigma(W_\lambda)$ (Å)	$N(\text{H}_3^+)$ (10 $^{14}$ cm $^{-2}$ )	$\sigma(N)$ (10 $^{14}$ cm $^{-2}$ )
HD 20041	$R(1, 1)^u$	-1.4	8.4	0.017	0.004	0.70	0.15
	$R(1, 0)$	-1.5	9.6	0.036	0.004	0.91	0.10
HD 21389	$R(1, 1)^u$	-1.9	11.9	0.009	0.002	0.39	0.07
	$R(1, 0)$	-0.2	15.6	0.016	0.002	0.41	0.05
$\zeta$ Per	$R(1, 1)^u$	7.5	9.7	0.010	0.001	0.43	0.05
	$R(1, 0)$	6.8	8.8	0.010	0.001	0.26	0.03
X Per	$R(1, 1)^u$	8.3	11.6	0.011	0.002	0.46	0.10
	$R(1, 0)$	5.7	9.6	0.012	0.002	0.31	0.06
HD 169454	$R(1, 1)^u$	2.6	11.1	0.005	0.002	0.21	0.08
	$R(1, 0)$	2.1	10.8	0.014	0.002	0.35	0.05
HD 229059	$R(1, 1)^u$	5.9	12.2	0.058	0.003	2.42	0.14
	$R(1, 0)$	4.4	12.4	0.059	0.003	1.48	0.09
BD -14 5037	$R(1, 1)^u$	17.6	9.6	0.010	0.003	0.40	0.13
	$R(1, 0)$	18.6	10.4	0.009	0.003	0.23	0.08
W40 IRS 1a	$R(1, 1)^u$	7.5	10.8	0.051	0.008	2.12	0.33
	$R(1, 0)$	8.2	6.6	0.050	0.006	1.26	0.16
HD 21483	$R(1, 1)^u$	...	10	<0.036	...	<1.53	...
	$R(1, 0)$	...	10	<0.036	...	<0.93	...
40 Per	$R(1, 1)^u$	...	10	<0.015	...	<0.60	...
	$R(1, 0)$	...	10	<0.015	...	<0.36	...
$\sigma$ Per	$R(1, 1)^u$	...	10	<0.009	...	<0.42	...
	$R(1, 0)$	...	10	<0.009	...	<0.27	...
$\epsilon$ Per	$R(1, 1)^u$	...	10	<0.009	...	<0.39	...
	$R(1, 0)$	...	10	<0.009	...	<0.24	...
$\xi$ Per	$R(1, 1)^u$	...	10	<0.009	...	<0.33	...
	$R(1, 0)$	...	10	<0.009	...	<0.21	...
62 Tau	$R(1, 1)^u$	...	10	<0.045	...	<1.89	...
	$R(1, 0)$	...	10	<0.045	...	<1.14	...
Red Rectangle	$R(1, 1)^u$	...	10	<0.006	...	<0.21	...
	$R(1, 0)$	...	10	<0.006	...	<0.15	...

Table 3—Continued

Object	Transition	$v_{\text{LSR}}$ (km s $^{-1}$ )	FWHM (km s $^{-1}$ )	$W_\lambda$ (Å)	$\sigma(W_\lambda)$ (Å)	$N(\text{H}_3^+)$ (10 $^{14}$ cm $^{-2}$ )	$\sigma(N)$ (10 $^{14}$ cm $^{-2}$ )
$\sigma$ Sco	$R(1, 1)^u$	...	10	<0.009	...	<0.36	...
	$R(1, 0)$	...	10	<0.009	...	<0.21	...
HD 147889	$R(1, 1)^u$	...	10	<0.009	...	<0.39	...
	$R(1, 0)$	...	10	<0.009	...	<0.24	...
$\zeta$ Oph	$R(1, 1)^u$	...	10	<0.003	...	<0.18	...
	$R(1, 0)$	...	10	<0.003	...	<0.12	...
HD 168625	$R(1, 1)^u$	...	10	<0.012	...	<0.54	...
	$R(1, 0)$	...	10	<0.012	...	<0.33	...
$\lambda$ Cep	$R(1, 1)^u$	...	10	<0.012	...	<0.54	...
	$R(1, 0)$	...	10	<0.012	...	<0.33	...

Note. —  $v_{\text{LSR}}$  is the observed line of sight velocity in the local standard of rest frame. FWHM is the line full width at half maximum (for the purpose of calculating column density upper limits, the FWHM is assumed to be 10 km s $^{-1}$  for all spectra without absorption lines).  $W_\lambda$  is the equivalent width of the line in Ångströms.  $\sigma(W_\lambda)$  is the one standard deviation uncertainty of the equivalent width. Upper limits for the equivalent width were found by taking 3 $\times$  $\sigma(W_\lambda)$ .  $N(\text{H}_3^+)$  is the H $_3^+$  column density.  $\sigma(N)$  is the one standard deviation uncertainty of the H $_3^+$  column density. Upper limits for the column density were found by taking 3 $\times$  $\sigma(N)$ .

Table 4. Sightline Parameters

Object	$N(\text{H}_3^+)_\text{tot}$ ( $10^{14} \text{ cm}^{-2}$ )	$\sigma(N)$ ( $10^{14} \text{ cm}^{-2}$ )	$T(\text{H}_3^+)$ (K)	$E(B - V)$ (mag)	$N_\text{H}$ ( $10^{21} \text{ cm}^{-2}$ )	$f$	$n_\text{H}$ ( $\text{cm}^{-3}$ )	$L$ (pc)	$\zeta_p$ ( $10^{-16} \text{ s}^{-1}$ )
HD 20041	1.6	0.18	76 <sup>c</sup>	0.72 <sup>d</sup>	4.18 <sup>m</sup>	0.67 <sup>q</sup>	250 <sup>t</sup>	5.4	2.9
HD 21389	1.0	0.08	51	0.57 <sup>d</sup>	3.31 <sup>m</sup>	0.67 <sup>q</sup>	250 <sup>t</sup>	4.3	1.8
$\zeta$ Per	0.7	0.06	28	0.31 <sup>d</sup>	1.59 <sup>n o</sup>	0.60 <sup>r</sup>	215 <sup>u</sup>	2.4	3.2
X Per	0.8	0.17	30	0.59 <sup>d</sup>	2.20 <sup>n p</sup>	0.76 <sup>r</sup>	325 <sup>u</sup>	2.2	3.1
HD 169454	0.6	0.09	180 <sup>c</sup>	1.12 <sup>d</sup>	6.50 <sup>m</sup>	0.50 <sup>s</sup>	265 <sup>u</sup>	7.9	0.9
HD 229059	3.9	0.16	28	1.71 <sup>d</sup>	9.92 <sup>m</sup>	0.67 <sup>q</sup>	250 <sup>t</sup>	13	2.9
BD -14 5037	0.6	0.16	26	1.55 <sup>e</sup>	8.99 <sup>m</sup>	0.67 <sup>q</sup>	250 <sup>t</sup>	12	0.5
W40 IRS 1a	3.4	0.37	27	2.90 <sup>f</sup>	16.8 <sup>m</sup>	0.67 <sup>q</sup>	250 <sup>t</sup>	22	1.5
WR 104	2.3 <sup>a</sup>	0.25 <sup>a</sup>	38 <sup>a</sup>	2.10 <sup>g</sup>	12.2 <sup>m</sup>	0.67 <sup>q</sup>	250 <sup>t</sup>	16	1.4
WR 118	6.5 <sup>a</sup>	0.18 <sup>a</sup>	40 <sup>a</sup>	4.13 <sup>g</sup>	24.0 <sup>m</sup>	0.67 <sup>q</sup>	250 <sup>t</sup>	31	2.0
WR 121	2.2 <sup>a</sup>	0.28 <sup>a</sup>	...	1.68 <sup>g</sup>	9.74 <sup>m</sup>	0.67 <sup>q</sup>	250 <sup>t</sup>	13	1.7
Cyg OB2 12	3.8 <sup>a</sup>	0.36 <sup>b</sup>	27 <sup>a</sup>	3.35 <sup>h</sup>	19.4 <sup>m</sup>	0.67 <sup>q</sup>	300 <sup>v</sup>	21	1.8
Cyg OB2 5	2.6 <sup>a</sup>	0.19 <sup>a</sup>	47 <sup>a</sup>	1.99 <sup>h</sup>	11.5 <sup>m</sup>	0.67 <sup>q</sup>	225 <sup>v</sup>	17	1.5
HD 183143	2.3 <sup>a</sup>	0.08 <sup>a</sup>	31 <sup>a</sup>	1.28 <sup>i</sup>	7.42 <sup>m</sup>	0.67 <sup>q</sup>	250 <sup>t</sup>	9.6	2.3
HD 21483	<2.2	...	...	0.56 <sup>d</sup>	3.25 <sup>m</sup>	0.67 <sup>q</sup>	250 <sup>t</sup>	4.2	<5.7
40 Per	<0.9	...	...	0.24 <sup>j</sup>	1.67 <sup>n o</sup>	0.35 <sup>r</sup>	80 <sup>w</sup>	6.7	<2.6
$\alpha$ Per	<0.6	...	...	0.31 <sup>d</sup>	1.52 <sup>n o</sup>	0.54 <sup>r</sup>	265 <sup>u</sup>	1.9	<5.0
$\epsilon$ Per	<0.5	...	...	0.09 <sup>j</sup>	0.35 <sup>n o</sup>	0.19 <sup>r</sup>	15 <sup>x</sup>	7.5	<2.4
$\xi$ Per	<0.5	...	...	0.33 <sup>d</sup>	1.82 <sup>n o</sup>	0.38 <sup>r</sup>	300 <sup>x</sup>	2.0	<4.5
62 Tau	<2.7	...	...	0.37 <sup>d</sup>	2.19 <sup>n p</sup>	0.56 <sup>r</sup>	280 <sup>u</sup>	2.5	<14
$\alpha$ Sco	<0.5	...	...	0.73 <sup>e</sup>	4.23 <sup>m</sup>	0.67 <sup>q</sup>	225 <sup>v</sup>	6.1	<0.9
HD 147889	<0.6	...	...	1.07 <sup>d</sup>	6.21 <sup>m</sup>	0.67 <sup>q</sup>	525 <sup>v</sup>	3.8	<1.6
$\zeta$ Oph	<0.3	...	...	0.32 <sup>d</sup>	1.40 <sup>n o</sup>	0.65 <sup>r</sup>	215 <sup>u</sup>	2.1	<1.5
HD 168625	<0.8	...	...	1.48 <sup>e</sup>	8.58 <sup>m</sup>	0.67 <sup>q</sup>	250 <sup>t</sup>	11	<0.8
$\lambda$ Cep	<0.8	...	...	0.57 <sup>d</sup>	2.80 <sup>n p</sup>	0.49 <sup>r</sup>	115 <sup>u</sup>	7.8	<1.3
HD 168607	<0.6 <sup>a</sup>	...	...	1.61 <sup>i</sup>	9.34 <sup>m</sup>	0.67 <sup>q</sup>	250 <sup>t</sup>	12	<0.5
HD 194279	<1.2 <sup>a</sup>	...	...	1.22 <sup>i</sup>	7.08 <sup>m</sup>	0.67 <sup>q</sup>	250 <sup>t</sup>	9.1	<1.3

| 32 |

Table 4—Continued

Object	$N(\text{H}_3^+)_\text{tot}$ ( $10^{14} \text{ cm}^{-2}$ )	$\sigma(N)$ ( $10^{14} \text{ cm}^{-2}$ )	$T(\text{H}_3^+)$ (K)	$E(B - V)$ (mag)	$N_\text{H}$ ( $10^{21} \text{ cm}^{-2}$ )	$f$	$n_\text{H}$ ( $\text{cm}^{-3}$ )	$L$ (pc)	$\zeta_p$ ( $10^{-16} \text{ s}^{-1}$ )
$\chi^2$ Ori	<0.7 <sup>a</sup>	...	...	0.44 <sup>k</sup>	2.55 <sup>m</sup>	0.67 <sup>q</sup>	250 <sup>t</sup>	3.3	<2.1
P Cyg	<0.6 <sup>a</sup>	...	...	0.63 <sup>l</sup>	3.65 <sup>m</sup>	0.67 <sup>q</sup>	250 <sup>t</sup>	4.7	<1.2

Note. —  $N(\text{H}_3^+)_\text{tot}$  is total  $\text{H}_3^+$  column density.  $\sigma(N)$  is one standard deviation uncertainty of the total column density. Upper limits for the column density were found by taking  $3 \times \sigma(N)$ .  $T(\text{H}_3^+)$  is the excitation temperature of  $\text{H}_3^+$  as determined from the column densities of the (1,0) and (1,1) states.  $E(B - V)$  is the color excess.  $N_\text{H}$  is the column density of hydrogen nuclei.  $f$  is the molecular hydrogen fraction.  $n_\text{H}$  is the number density of hydrogen nuclei.  $L$  is the cloud path length assuming a uniform distribution of gas.  $\zeta_p$  is the primary cosmic-ray ionization rate. Upper limits on  $\zeta_p$  were calculated using  $3 \times \sigma(N)$ .

<sup>a</sup>from McCall et al. (2002)

<sup>b</sup>from McCall et al. (1998)

<sup>c</sup>these high temperatures are most likely caused by inaccurate measurements of the (1,1) state column density due to atmospheric interference

<sup>d</sup>from Thorburn et al. (2003)

<sup>e</sup>derived from method used in Thorburn et al. (2003)

<sup>f</sup>derived from Shuping et al. (1999) assuming  $R_V = A_V/E(B - V) = 3.1$

<sup>g</sup>derived from Pendleton et al. (1994) assuming  $R_V = A_V/E(B - V) = 3.1$

<sup>h</sup>from Schulte (1958)

<sup>i</sup>from Snow et al. (1977)

<sup>j</sup>from Savage et al. (1977)

<sup>k</sup>derived from intrinsic color of Wegner (1994)

<sup>l</sup>from Lamers et al. (1983)

<sup>m</sup>calculated from  $N_{\text{H}} \approx E(B - V) \times 5.8 \times 10^{21} \text{ cm}^{-2} \text{ mag}^{-1}$  in Bohlin et al. (1978)

<sup>n</sup>calculated from observed H and H<sub>2</sub> column densities

<sup>o</sup>from B. Rachford (private communication)

<sup>p</sup>from Rachford et al. (2002)

<sup>q</sup>we adopt  $f = 0.67$  for sightlines without measured column densities

<sup>r</sup>H<sub>2</sub> fraction derived from same sources as column densities

<sup>s</sup> $f = 0.5$  assumed by Sonnentrucker et al. (2007) when calculating  $n_{\text{H}}$

<sup>t</sup>adopted number density

<sup>u</sup>from Sonnentrucker et al. (2007)

<sup>v</sup>from  $n(\text{H} + \text{H}_2)$  in Sonnentrucker et al. (2007) assuming  $f = 0.67$

<sup>w</sup>derived from pressure in Jenkins et al. (1983)

<sup>x</sup>from Jura (1975)

Table 5. Primary Cosmic-ray Ionization Rate,  $\zeta_p$  ( $10^{-16}$  s $^{-1}$ ), for Select Sightlines

reference	$\zeta$ Per	$\sigma$ Per	$\epsilon$ Per	$\xi$ Per	$\zeta$ Oph
1	3.2	<5.0	<2.4	<4.5	<1.5
2	0.22	2.50	0.01	0.06	0.17
3	0.17	1.30	...	$\leq$ 0.26	...
4	1-2	$\geq$ 8	...	...	$\geq$ 4
5	5.2	...	...	...	...
6	2.5	...	...	...	...

Note. — The upper limits from this paper are calculated using the  $3\sigma$  uncertainty in the H<sub>3</sub><sup>+</sup> column density. The value from McCall et al. (2003) is found by using the conversion factor given in equation (10).

References. — (1) this paper; (2) Hartquist et al. (1978b); (3) Federman et al. (1996); (4) van Dishoeck & Black (1986); (5) McCall et al. (2003); (6) Le Petit et al. (2004)